Finite-size energy gap in weak and strong topological insulators

Ken-Ichiro Imura,[1] Mayuko Okamoto,[1] Yukinori Yoshimura,[1] Yositake Takane,[1] and Tomi Ohtsuki[2]

[1]*Department of Quantum Matter, AdSM, Hiroshima University, Higashi-Hiroshima 739-8530, Japan*
[2]*Department of Physics, Sophia University, 102-8554 Tokyo, Japan*

The nontrivialness of a topological insulator (TI) is characterized either by a bulk topological invariant or by the existence of a protected metallic surface state. Yet, in realistic samples of finite size, this nontrivialness does not necessarily guarantee the *gaplessness* of the surface state. Depending on the geometry and on the topological indices, a finite-size energy gap of different nature can appear, and, correspondingly, exhibit various scaling behaviors of the gap. The spin-to-surface locking provides one such gap-opening mechanism, resulting in a power-law scaling of the energy gap. Weak and strong TIs show different degrees of sensitivity to the geometry of the sample. As a noteworthy example, a strong TI nanowire of a rectangular-prism shape is shown to be more gapped than that of a weak TI of precisely the same geometry.

I. INTRODUCTION

The nontrivialness of a topological insulator (TI) is often characterized by the presence of a gapless surface state.[1,2] A one-to-one correspondence can be established between the (non)trivialness of a bulk topological invariant and the presence vs absence of the gapless surface state (bulk-surface correspondence). However, precisely speaking, for such a gapless state to exist, both the trivial and nontrivial sides are semi-infinite, separated by an infinitely large interface. The above distinction can be made, therefore, only in such an idealized situation. TI samples, in reality, occupy only a finite domain of the space, and also have a variety of shapes surrounded generally by a curved or folded surface(s). In experiments, it is also the case that some TI samples of nanometer scale size exhibit a clear gapless surface state, while other samples of the same chemical composition but of a different geometrical shape do not necessarily exhibit a clear signature of topological nontriviality. Such an issue will be addressed in this paper.

The main scope of the paper is concomitant with the observation that there are three different gap-opening mechanisms effective in the samples of finite size. The most primitive among them is the one due to mixing of the surface electronic wave functions on the opposing sides, e.g., of an infinitely large slab-shaped sample. Such an energy gap, associated with the finite thickness of the gapped bulk, decays exponentially as a function of the thickness of the slab and is, in practice, almost irrelevant except in extremely thin film samples.[3] The low-energy (surface) electronic spectrum in the slab geometry suffers, indeed, only from this type of exponentially small finite-size energy gap.[4–7] The second mechanism to open a gap in the surface electronic spectrum, which is also more relevant in magnitude, is the so-called spin-to-surface locking.[8–11] The electronic spin in the *a priori* gapless surface state on a curved surface of TI has a tendency to be locked in-plane to the local tangent of the surface. In the cylindrically symmetric case, the spin-to-surface locking results in the *half-integral* quantization of the orbital angular momentum along the axis of the cylinder. The half-odd integer quantization gaps out the spectrum, and this gap decays only algebraically; it is qualitatively more relevant than the gap of the previous type.

Indeed, the spin-to-surface locking leads to opening of the gap, irrespective of the presence of cylindrical symmetry, e.g., in a prism-shaped sample.

Another aspect of the topological insulator which we aim to explore in this paper is the role of anisotropy, especially in the weak topological insulator (WTI) phase. This is strongly related to the third mechanism of gap opening, which occurs due to the interplay of the anisotropy of WTI and the specific geometry that we will focus on (i.e., the case of the prism-shaped geometry). In three spatial dimensions (3D), the $\mathbb{Z}_2$ topological insulator is known to be characterized by four $\mathbb{Z}_2$ indices,[12–14] the principal (strong) index ν_0, and other "weak" indices ν_1, ν_2, ν_3, instead of a single $\mathbb{Z}_2$ index in the case of 2D. The principal index ν_0 is used to distinguish a strong topological insulator (STI) ($\nu_0 = 1$) from trivial and weak topological insulators ($\nu_0 = 0$). In a WTI, at least one of its weak indices exhibits a nontrivial value ($=1$). A WTI shows generally an even number of helical Dirac cones on its surfaces, but on the surface normal to its "weak vector," $\vec{\nu} = (\nu_1, \nu_2, \nu_3)$, it shows no Dirac cone. The WTI can be viewed as stacked layers of 2D $\mathbb{Z}_2$ topological insulators. In this regard, the set of weak indices $(\nu_1 \nu_2 \nu_3)$ can be regarded as the Miller index of such stacked layers. Since gapless surface states are expected to form only at the edge of the stacked layers, one can naturally understand that no Dirac cone is formed on a surface normal to $\vec{\nu}$ in this picture. To summarize, the WTI bears two Dirac cones on surfaces *parallel* to $\vec{\nu}$ and no Dirac cone on surfaces *normal* to $\vec{\nu}$. When this characteristic feature is combined with the specific (rectangular) prism geometry, the anisotropy of a WTI manifests as an alternating size dependence of the energy gap; the magnitude of the gap is qualitatively different whether the number of "stacked layers" is even or odd. It will be demonstrated that weak and strong TIs show different degrees of sensitivity to the geometry of the sample.

The periodic table of topological insulators and superconductors classifies them by the nature of strong indices characterizing the system. The weak indices are not shown, at least explicitly on the table.[15,16] Showing an even number of Dirac cones on its surfaces, WTI is *a priori* considered not to be robust. But recently, a few counter examples to this common

belief have been proposed. One is the existence of protected gapless helical modes along a dislocation line in the WTI.[17,18] More recently, a couple of papers have demonstrated that an even number of Dirac cones on the surface of WTI are actually not that fragile against disorder.[19,20] Here, we point out that in a specific situation in the prism-shaped geometry, the surface state of a WTI is, in a sense, "more strongly protected" from a finite-size energy gap than that of a STI.

The paper is organized as follows. In Sec. II, we introduce our effective model Hamiltonian for 3D anisotropic topological insulators. The phase diagram of the model is determined by the calculation of topological numbers in the bulk. In Sec. III, we discuss different origins of the finite-size energy gap, highlighting the role of spin-to-surface locking in the cylindrical geometry. In Sec. IV, we demonstrate that in the more realistic rectangular-prism geometry, three types of gap opening appear and disappear by a small change of model parameters, leading to an intricate size dependence of the gap. Section V is devoted to conclusions.

II. MODEL AND ITS PHASE DIAGRAM—ENGINEERING THE WEAK INDICES

As a concrete realization of strong and weak topological insulators with specific strong and weak indices, ν_0 and $\vec{\nu} = (\nu_1, \nu_2, \nu_3)$, we consider, as given in Eq. (1), a Wilson-Dirac-type effective Hamiltonian for a 3D topological insulator implemented on a cubic lattice.[21,22] Since we will be interested in the analysis of WTI phases with anisotropic weak indices, we choose the mass parameters m_{2x}, m_{2y}, m_{2z} appearing in the Wilson term [see Eq. (2)] to be anisotropic.

A. The Wilson-Dirac-type effective Hamiltonian

Let us consider the following Wilson-Dirac-type effective Hamiltonian for a 3D topological insulator implemented on a cubic lattice:

$$H_{\text{bulk}} = \epsilon(\boldsymbol{k})\mathbf{1} + \tau_x m(\boldsymbol{k}) + \tau_y \sigma_\mu A_\mu \sin k_\mu, \quad (1)$$

where $\epsilon(\boldsymbol{k})$ is an even function of $\boldsymbol{k}$, and

$$m(\boldsymbol{k}) = m_0 + 2m_{2\mu}(1 - \cos k_\mu). \quad (2)$$

In Eqs. (1) and (2), a summation over the repeated index μ (= x,y,z) is not shown explicitly. The model specified by this couple of equations can be regarded as a tight-binding model with only the nearest neighbor hopping, determining the structure of the energy bands over the entire 3D Brillouin zone (BZ). Equation (1) can be regarded as a 4×4 matrix, spanned by two types of Pauli matrices $\boldsymbol{\sigma}$ and $\boldsymbol{\tau}$, each representing physically real and orbital spins, respectively. Compared with a more generic representation of the Dirac Hamiltonian in terms of the "$\boldsymbol{\gamma}$ matrices," we have chosen in Eq. (1) "γ_0" coupled to the mass term $m(\boldsymbol{k})$ associated only with an *orbital* spin τ_x.

The mass term (2) represents (a half of) the band gap at time-reversal invariant momenta (TRIM), $\boldsymbol{k} = \boldsymbol{k}_0$, satisfying $-\boldsymbol{k}_0 = \boldsymbol{k}_0 + \boldsymbol{G}$, with $\boldsymbol{G}$ being a reciprocal lattice vector, corresponding either to a normal or an inverted gap, depending on the relative sign of m_0 and the coefficient of the quadratic (Wilson) term at a given TRIM. By investigating this feature

of band inversion at the eight TRIM as varying the mass parameters, one can identify[23] various weak and strong TI phases characterized by strong and weak indices, ν_0 and $\vec{\nu} = (\nu_1, \nu_2, \nu_3)$. Phase boundaries between such topologically distinguishable insulating phases correspond necessarily to closing of the bulk energy gap.

Known examples of 3D topological insulators are layered materials, exhibiting, in the leading-order approximation, uniaxial anisotropy in the crystal c axis.[24–28] To reflect this feature in the effective tight-binding model, i.e., in Eqs. (1) and (2), we assume that our model parameters have the same uniaxial anisotropy.[21] In particular, the three mass parameters m_{2x}, m_{2y}, and m_{2z} are classified into two types, $m_{2\parallel}$ and $m_{2\perp}$, depending on whether the corresponding hopping direction is *parallel* or *perpendicular* to the stacked layers of the crystal. Clearly, the correspondence depends on the relative orientation of the crystal growth axis and our Cartesian coordinates; e.g., when the crystal c axis is oriented to the direction of the z axis,

$$m_{2\perp} = m_{2z}, \quad m_{2\parallel} = m_{2x} = m_{2y},$$
$$A_\perp = A_z, \quad A_\parallel = A_x = A_y. \quad (3)$$

Independently of this choice of the relative orientation, our control parameters for specifying topologically different phases are relative magnitudes of m_0, $m_{2\perp}$, and and $m_{2\parallel}$. Then, by studying the feature of band inversion at eight TRIM as a function of these control parameters,[23] one can deduce the phase diagram of the model. Figure 1 shows such a phase diagram depicted in the $(m_0/m_{2\parallel}, m_{2\perp}/m_{2\parallel})$ plane.

B. Phase diagram

Figure 1 shows the phase diagram of the Wilson-Dirac-type effective tight-binding Hamiltonian given in Eqs. (1) and (2). The uniaxial anisotropy of the hopping parameters, as given by Eqs. (3), is taken into account. Each of the STI and WTI phases are characterized by four $\mathbb{Z}_2$ indices. The calculated winding number N_3 (see Appendix A) is also shown. Solid lines, separating neighboring topologically distinct phases, indicate closing of the bulk energy gap. Duplicate lines appearing at the phase boundary correspond to simultaneous formation of two bulk 3D Dirac cones. The duplication is due to the uniaxial choice of the hopping parameters. To see such specific features, let us focus below on a few particular examples of the STI and WTI phases.

Let us first concentrate on the isotropic line $m_{2\perp}/m_{2\parallel} = 1$ in the phase diagram (indicated as a thick green line in Fig. 1). The change of the winding number N_3 on this line is shown in Fig.11(a). Notice that on this line, different STI and WTI phases show only symmetric weak indices. At the phase boundaries between the STI and WTI phases, a double and single solid lines cross, indicating simultaneous closing of three Dirac cones in the bulk. This occurs at X, Y, Z: $\boldsymbol{k}_X = (\pi,0,0)$, $\boldsymbol{k}_Y = (0,\pi,0)$, $\boldsymbol{k}_Z = (0,0,\pi)$, three symmetric points (TRIM) in the 3D BZ.

Stopping at $m_0/m_{2\parallel} = -1$, let us now vary $m_{2\perp}/m_{2\parallel}$, i.e., introduce anisotropy in the mass parameters. On the line $m_0/m_{2\parallel} = -1$ (thick red line in Fig. 1), the system is in a STI phase with $\nu_0 = 1$ and $\vec{\nu} = (0,0,0)$ when $m_{2\perp}/m_{2\parallel} > 1/4$. The anisotropy appears in the weak indices below this critical value, $m_{2\perp} = -m_0/4$, corresponding to band crossing that occurs at
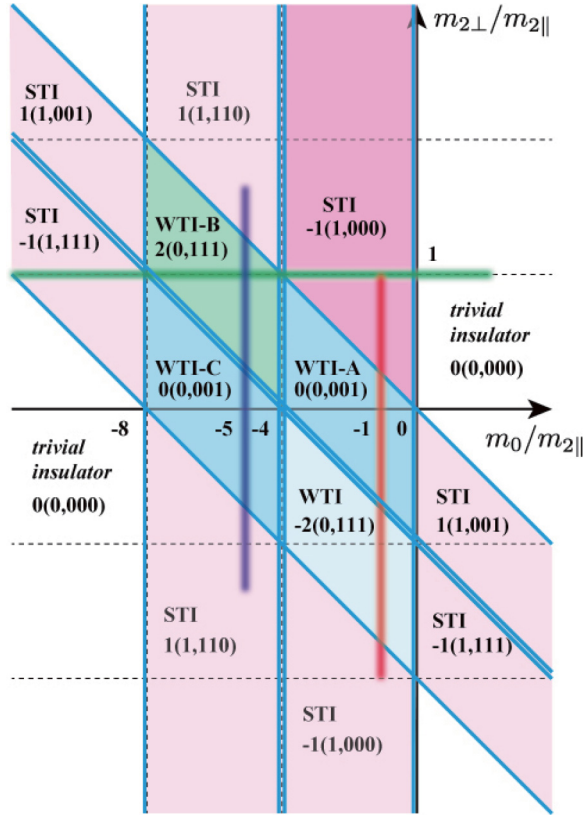
FIG. 1. (Color online) The phase diagram of the Wilson-Dirac-type effective tight-binding Hamiltonian given in Eqs. (1) and (2). Notice the anisotropy of our hopping parameters [see Eqs. (3)]. In each of the strong (STI) and weak (WTI) topological insulator phases, together with the nature of the specific phase, the four $\mathbb{Z}_2$ indices ν_j ($j = 0, 1, 2, 3$) and the winding number N_3 are shown, as $N_3(\nu_0, \nu_1\nu_2\nu_3)$ [See Eq. (A4) for the definition of N_3]. The solid lines representing the phase boundaries correspond to closing of the bulk energy gap.

the Z point, and the system enters a WTI-A phase with $\nu_0 = 0$ and $\vec{\nu} = (0,0,1)$ when $m_{2\perp}/m_{2\parallel} < 1/4$. In later sections, we will quantify various manifestations of this quantum phase transition in the finite-size effects. The situation is similar on the line $m_0/m_{2\parallel} = -5$ (thick blue line in Fig. 1), above and below the critical point $m_{2\perp}/m_{2\parallel} = 1/4$, although in this second example, the transition occurs from an isotropic to an anisotropic WTI phase, each named, respectively, the WTI-B and WTI-C phase.

III. DIFFERENT ORIGINS OF THE FINITE-SIZE ENERGY GAP

A single Dirac cone on the surface of a STI is topologically protected[2] and also robust against disorder.[29,30] In reality, TI samples always have a finite thickness between the two surfaces of opposing sides. Imagine a slab-shaped sample (cf. Table I), which we assume infinitely large, neglecting the existence of side surfaces. In such a slab geometry, STI bears a pair of surface Dirac cones, each localized in the vicinity of the two opposing surfaces. These two "Dirac cones" do not communicate, and consequently remain gapless, as far as the thickness of the slab is much larger than the penetration of the surface state into the bulk (see Appendix B for an extensive

TABLE I. Definition of the surfaceless, slab, (rectangular) prism, and cubic geometries. Here, to avoid confusion in the terminology, we define these different types of geometries in terms of the switching on and off of the periodic boundary conditions (PBCs) in the x, y, and z directions. In the Table, 1 and 0 signify that the PBC in the corresponding direction is, respectively, on and off. In the latter case, the PBC is replaced by the fixed boundary condition (FBC).

Geometry	x-PBC	y-PBC	z-PBC
Surfaceless	1	1	1
Slab	1	1	0
(Rectangular) prism	0	1	0
Cubic	0	0	0

discussion of the penetration of the surface wave function in the slab geometry; see also Refs. 4–7).

In a sense, this gaplessness is also protected by the very slab geometry. In the case of a sample of more realistic shape with typical side surfaces (cf. the cases of a prism and a cube; see Table I), the same protection is no longer valid. The side surfaces open *a priori* gapless channels, allowing for communication between the two initial Dirac cones on two surfaces of the slab. Since this communication through gapless side surfaces is much stronger than the one through the gapped bulk (cf. the case of the slab geometry), it leads to opening of a size gap qualitatively more relevant than the latter case.

Of course, the effects of such side surfaces appear in the transport characteristics only when an electron can really "see" the ends of the sample. In a macroscopic sample in which the (single-particle) relaxation length, determined, e.g., by the inelastic scattering length, does not exceed the size of the system, finite-sizes effects corresponding to a length scale smaller than the former are naturally smeared out. In the following sections, we consider nanowire samples that have a nanometer-scale cross section, with its circumference sufficiently smaller than the relaxation length. Here, we concentrate on the cylindrical geometry, imposing additionally a rotational (cylindrical) symmetry. We also assume that the system is extended to infinity or (by taking only two of four end surfaces into account) periodic in the remaining direction. A symptom of the effects we discuss in this section may be observed experimentally in a transport measurement analogous to the one in Ref. 31.

A. Spin-to-surface locking on the cylindrical surface

The protected surface state of a topological insulator is often cited with another adjective: helical. The word helical stems from a specific feature, often referred to as spin-to-momentum locking,[32] that the helical state exhibits in momentum space. Here, we highlight another characteristic of the helical surface state, the "spin-to-surface locking," which manifests in *real* space and when the surface is curved. The electronic spin in a helical state on such a curved surface is shown to be locked in-plane to the local tangent of the surface.[8–11]

The spin-to-surface locking can be also regarded as a consequence of the (spin) Berry phase of π. In the case of rotationally symmetric (cylindrical) wire, the orbital angular

momentum along the axis of the wire is quantized to be *half-odd* integers. This half-odd integral quantization gaps out the spectrum of electronic motion along the wire. The spin-to-surface locking leads, indeed, irrespective of the presence of rotational symmetry, to opening of the Dirac spectrum.

To be explicit, let us consider the continuum limit of Eqs. (1) and (2), or an effective $\boldsymbol{k} \cdot \boldsymbol{p}$ Hamiltonian at the Γ point ($\boldsymbol{k} = \boldsymbol{0}$),

$$H_{\text{bulk}} = \epsilon(\boldsymbol{p})\mathbf{1} + \tau_x m(\boldsymbol{p}) + A\tau_y \sigma_\mu p_\mu, \qquad (4)$$

where $m(\boldsymbol{p}) = m_0 + m_2 \boldsymbol{p}^2$. Here, we focus on the isotropic case: $m_{2\mu} = m_2$ and $A_\mu = A$ for $\mu = x, y, z$. We also assume $\epsilon(\boldsymbol{p}) = 0$, for simplicity. We then consider the eigenvalue problem for Eq. (4), i.e.,

$$H_{\text{bulk}}|\psi\rangle\!\rangle = E|\psi\rangle\!\rangle, \qquad (5)$$

in the cylindrical coordinates:

$$r = \sqrt{x^2 + y^2}, \quad \phi = \arctan \frac{y}{x}. \qquad (6)$$

Note that our TI sample occupies the interior of a cylinder of radius R. As shown in Appendix C, any surface solutions $|\boldsymbol{\alpha}\rangle\!\rangle$ of Eq. (5) can be expressed as a linear combination of the two basis solutions,

$$|\boldsymbol{r}+\rangle\!\rangle_{\text{dv}} = \rho(r)|\tau_z+\rangle|\boldsymbol{r}+\rangle_{\text{dv}}, \quad |\boldsymbol{r}-\rangle\!\rangle_{\text{dv}} = \rho(r)|\tau_z-\rangle|\boldsymbol{r}-\rangle_{\text{dv}}, \qquad (7)$$

where $|\tau_z\pm\rangle$ is an eigenstate of τ_z with the corresponding eigenvalue ± 1 and

$$|\boldsymbol{r}\pm\rangle_{\text{dv}} = \frac{1}{\sqrt{2}}\begin{bmatrix} e^{-i\phi/2} \\ \pm e^{i\phi/2} \end{bmatrix} \qquad (8)$$

are two real-spin eigenstates pointing either to the centrifugal ($+\boldsymbol{r}$) or to the centripetal ($-\boldsymbol{r}$) direction. In Eqs. (7), $\rho(r)$ is the radial part of the surface wave function localized in the vicinity of the surface of the cylinder, given explicitly in Eq. (C12). In Eqs. (7) and (8), the subscript dv is added to make explicit that these spinors are double valued. In terms of $|\boldsymbol{r}\pm\rangle\!\rangle_{\text{dv}}$, the surface solution $|\boldsymbol{\alpha}\rangle\!\rangle$ reads

$$|\boldsymbol{\alpha}\rangle\!\rangle = \alpha_+(\phi)|\boldsymbol{r}+\rangle\!\rangle_{\text{dv}} + \alpha_-(\phi)|\boldsymbol{r}-\rangle\!\rangle_{\text{dv}}. \qquad (9)$$

Here, the explicit form of the coefficients $\alpha_\pm(\phi)$ is determined by solving the eigenvalue problem for the following surface effective Hamiltonian:

$$H_{\text{surf}} = A\left[-\frac{1}{R}\left(-i\frac{\partial}{\partial\phi}\right)\sigma_x + p_z\sigma_y\right], \qquad (10)$$

i.e.,

$$H_{\text{surf}}\boldsymbol{\alpha}(\phi) = E\boldsymbol{\alpha}(\phi), \qquad (11)$$

where

$$\boldsymbol{\alpha}(\phi) = \begin{bmatrix} \alpha_+(\phi) \\ \alpha_-(\phi) \end{bmatrix}. \qquad (12)$$

Notice here that thanks to the rotational symmetry with respect to the axis of the cylinder, the orbital angular momentum L_z is a good quantum number, which can be simultaneously diagonalized with H_{surf} and p_z. In the following, we focus on

such surface eigenstates of L_z, which can be represented in terms of $\boldsymbol{\alpha}(\phi)$ introduced in Eqs. (11) and (12) as

$$\boldsymbol{\alpha}(\phi) = \boldsymbol{\alpha}_{L_z, p_z}(\phi) = \begin{bmatrix} \alpha_+(\phi) \\ \alpha_-(\phi) \end{bmatrix} = e^{iL_z\phi}\begin{bmatrix} \alpha_+(0) \\ \alpha_-(0) \end{bmatrix}. \qquad (13)$$

Here, $\alpha_\pm(0)$ is specified by the orientation of the surface crystal momentum specified by p_z and $p_\phi = L_z/R$. The corresponding eigenenergy E of H_{surf} is then specified by p_ϕ and p_z as

$$E = E(p_\phi, p_z) = \pm A\sqrt{p_\phi^2 + p_z^2}. \qquad (14)$$

The state $|\boldsymbol{\alpha}\rangle\!\rangle$ thus given, and specified by the $\boldsymbol{\alpha}(\phi)$ given in Eq. (9), signifies a simultaneous eigenstate of H_{bulk}, L_z, and p_z, which may be also represented as $|L_z, p_z\rangle\!\rangle$. Equation (9) implies that such a state is an equal-weight superposition of the centrifugal and the centripetal spin components given in Eqs. (8), since $|\alpha_+(0)| = |\alpha_-(0)|$. This signifies that when an electron is on the surface of the cylinder at an angle ϕ in the configuration space, its spin state is constrained onto the local tangent of the cylinder at this position (spin-to-surface locking). While an electron travels around the cylinder in the configuration space, the corresponding spin frame also completes a 2π rotation in the spin space.

B. Half-integral quantization of the orbital angular momentum and the resulting finite-size energy gap

Let us reconsider the statue of the angle ϕ in different steps of the formulation. In the original bulk effective Hamiltonian (4), the angle ϕ purely specifies the position of an electron in the configuration space. This is also the case in its eigenstate $|\boldsymbol{\alpha}\rangle\!\rangle$. Therefore, $|\boldsymbol{\alpha}\rangle\!\rangle$ must be single valued with respect to the 2π rotation of ϕ,

$$|\boldsymbol{\alpha}\rangle\!\rangle|_{\phi\to\phi+2\pi} = |\boldsymbol{\alpha}\rangle\!\rangle. \qquad (15)$$

On the contrary, ϕ in $|\boldsymbol{r}\pm\rangle_{\text{dv}}$ specifies the direction of real $\mathbb{SU}(2)$ spin. Therefore, $|\boldsymbol{r}\pm\rangle\!\rangle_{\text{dv}}$ is double valued with respect to the 2π rotation of ϕ,

$$|\boldsymbol{r}\pm\rangle\!\rangle_{\text{dv}}|_{\phi\to\phi+2\pi} = -|\boldsymbol{r}\pm\rangle\!\rangle_{\text{dv}}. \qquad (16)$$

In Eq. (9), these two boundary conditions are compatible, only if

$$\boldsymbol{\alpha}(\phi + 2\pi) = -\boldsymbol{\alpha}(\phi), \qquad (17)$$

i.e., the coefficients $\alpha_\pm(\phi)$ are also antiperiodic. In light of Eq. (13), this requires

$$L_z = \pm\tfrac{1}{2}, \pm\tfrac{3}{2}, \ldots, \qquad (18)$$

i.e., the *orbital* angular momentum L_z is quantized to be half-odd integers.

Notice also that the double-valued quality of $|\boldsymbol{r}\pm\rangle\!\rangle_{\text{dv}}$ is not essential for the half-integral quantization of L_z. One can equally employ the single-valued version of Eq. (8),

$$|\boldsymbol{r}\pm\rangle_{\text{sv}} = \frac{1}{\sqrt{2}}\begin{bmatrix} 1 \\ \pm e^{i\phi} \end{bmatrix}, \qquad (19)$$

which is related to $|\boldsymbol{r}\pm\rangle\!\rangle_{\text{dv}}$ by a simple phase factor,

$$|\boldsymbol{r}\pm\rangle_{\text{sv}} = e^{i\phi/2}|\boldsymbol{r}\pm\rangle_{\text{dv}}. \qquad (20)$$

In this single-valued basis, the surface effective Hamiltonian acquires an additional phase factor π, the spin Berry phase, as

$$\widetilde{H}_{\text{surf}} = A \left[-\frac{1}{R} \left(-i \frac{\partial}{\partial \phi} + \frac{1}{2} \right) \sigma_x + p_z \sigma_y \right]. \qquad (21)$$

Then, if one employs the same representation (13) for the coefficients $\boldsymbol{\alpha}$, L_z takes formally integral values, $L_z = 0, \pm 1, \pm 2, \ldots$. The corresponding eigenenergy $E = E(p_\phi, p_z)$ can be also written formally in the same way as in Eq. (14). But, in that case, p_ϕ in the same formula must be reinterpreted as

$$p_\phi = \frac{L_z + 1/2}{R}. \qquad (22)$$

We have so far seen that whether one employs the double-valued [Eq. (8)] or the single-valued [Eq. (19)] basis, one finds, as expected, the same gapped spectrum given by Eq. (14) with either (i) $p_\phi = L_z / R$ with half-odd L_z [Eq. (18)], or (ii) p_ϕ given as in Eq. (22) with $L_z = 0, \pm 1, \pm 2, \ldots$. The magnitude of the energy gap is given by twice of

$$E_0 = E \left(\frac{1}{2R}, 0 \right) = \frac{A}{2R} \propto R^{-1}. \qquad (23)$$

This energy gap due to spin-to-surface locking, or eventually to the doubling of the original two Dirac cones through "side surfaces" of the cylinder, decays only *algebraically* as a function of (inversely proportional to) the circumference of the cylinder. This *enhanced* finite-size energy gap is in marked contrast to that of the slab due to mixing of the two surface wave functions sitting mainly on the opposing sides of the slab and separated by the bulk energy gap.

IV. CASE OF THE RECTANGULAR PRISM GEOMETRY

In the previous section, we have considered an idealized case of the cylindrical geometry to demonstrate how spin-to-surface locking leads to opening of the finite-size energy gap. With the rotational (cylindrical) symmetry hypothesized, the cylindrical geometry was best suited for analytic considerations of the surface state. Here, we attempt to realize an equivalent situation in numerical experiments in terms of the tight-binding simulation. For that purpose, we consider rather prism-shaped samples whose cross section on the plane normal to the axis of the (right) prism is a rectangle rather than a circle. From the viewpoint of topology, such a rectangular prism shape is a natural implementation[11] of the cylinderlike geometry on the cubic lattice.

In addition to that aspect as a substitute of a cylinder, there is also a more positive reason that we focus on this rectangular-prism geometry. In the previous section, through the comparison of the slab and cylinder, we have seen that preventing the communication of two Dirac cones sitting on the opposing sides of the sample helps protect the gaplessness of Dirac cones. We have so far discussed such switching on and off of this communication channel by changing the system's (global) geometry. Here, in this section, a new element comes into play: the weak indices. As mentioned in Sec. I, the weak indices have the potential to exclude a gapless Dirac cone from a surface oriented in a particular direction, i.e., that of the weak vector $\vec{v} = (v_1, v_2, v_3)$.

Folded surfaces of the rectangular-prism geometry are more adapted for implementing a weak vector as a means to eradicate the "dangerous" gapless channels from the targeted side surfaces. Another characteristic of the WTI surface state is that it exhibits an even number of Dirac cones. These two features combine to make the gaplessness of the surface state of a prism-shaped WTI a rather subtle issue, which depends intricately on the geometry and on the nature of weak indices. Depending on the relative orientation between the weak vector and the surfaces of the rectangular prism and on the size of the prism, noncompatibility of the surface wave function with a specific boundary condition imposed by the geometry leads to, or does not lead to, opening of a finite-size energy gap.

The system we consider here has a shape of rectangular prism extended in the $\hat{y}$ direction. We assume that the prism is infinitely long, or periodic, without end surfaces. Each cross section of the system at fixed y is restricted to a rectangular area of size $N_z \times N_x$ in the (z, x) plane:

$$1 \leqslant z \leqslant N_z, \quad 1 \leqslant x \leqslant N_x. \qquad (24)$$

The system has two surfaces ($\hat{x}$ surfaces) at $x = 1$ and $x = N_x$ normal to $\hat{x} = (1, 0, 0)$, and two others ($\hat{z}$ surfaces) at $z = 1$ and $z = N_z$ normal to $\hat{z} = (0, 0, 1)$. We assume translational symmetry in the $\hat{y}$ direction; k_y is a good quantum number. As for the anisotropy of bulk topological insulators, we consider the case of mass parameters with uniaxial-type anisotropy, as given in Eq. (3). In the WTI phase, this corresponds to the case of stacked 2D TI layers piled up in the z direction.

In the following, we will mainly focus on the WTI phase with a specific weak vector $\vec{v} = (0, 0, 1)$ normal to the $\hat{z}$ surfaces. Then, gapless Dirac cones are completely eliminated from these surfaces, at least in the limit of infinitely large surfaces. In the prism geometry (24), the wave function of the corresponding surface state has a finite amplitude only on $\hat{x}$ surfaces, and barely penetrates into the $\hat{z}$ side. The Dirac cones forced to be localized in each of the $\hat{x}$ surfaces are subject to a particular boundary condition imposed by this combination of the prism geometry and the weak vector. Compatibility or noncompatibility of the surface wave function with this specific boundary condition leads to an even/odd feature with respect to N_z (width of the $\hat{x}$ surfaces) of the finite-size energy gap in the WTI phase. After reviewing three typical situations that we encounter in the analysis of the size gap in the WTI and STI phases, we describe the nature of the even/odd feature in the spirit of the $k \cdot p$ approximation.

A. Even/odd feature in the WTI phase

The three typical situations we investigate are the cases of
(i) WTI with N_z even,
(ii) WTI with N_z odd, and
(iii) STI.
The three cases are also listed in Table II. In our model, given by Eqs. (1) and (2), and in the geometry employed, the three situations can be realized by a small change of parameters. As for the concrete choice of parameters, we use here the following double standard.[33] We first use the "theoretical values" that vary on the lines indicated in Fig. 1 for the demonstration of crossover from type (iii) to type (i), and from type (iii) to type (ii) behaviors. We believe that the use

TABLE II. Three typical behaviors of the finite-size energy gap in the rectangular-prism-shaped samples.

Cases	Type of phase	Parity of N_z	Size gap; N_z dependence	Gap-opening mechanism
(i)	WTI	even	N_z^{-1}	doubling of Dirac cones due to confinement
(ii)	WTI	odd	0 (exponentially small)	mixing of the opposing sides through gapped bulk
(iii)	STI	irrelevant	$(N_z + N_x)^{-1}$	spin-to-surface locking

of these theoretical values helps in understanding the nature of the phenomenon in light of the phase diagram. Then, in the actual computation of the size gap, we also use "experimental values" of the parameters that are deduced from experimental data for Bi_2Se_3.[21,34]

The three situations can be easily contrasted by the shape of the surface wave function. In the WTI phase (Figs. 2 and 3), the amplitude of the surface wave function concentrates on the two $\hat{x}$ surfaces. The weak vector $\vec{v}$ is here pointed in the direction $\hat{z}$, and expels the surface state from the sides normal to $\hat{z}$. In the STI phase (Fig. 4), on the contrary, the surface state is extended over all four surfaces. In these figures, the square of the total amplitude of the surface wave function,

$$|\psi(z,x)|^2 = \sum_{j=1}^{4} |\psi_j(z,x)|^2, \tag{25}$$

is plotted at each point on a cross section (the system is translationally invariant in the y direction).

Let us focus on more detailed structures of the shape of the surface wave function in the WTI phase, and compare the cases of N_z even (Fig. 2) and N_z odd (Fig. 3). On the two $\hat{x}$ surfaces, the wave function shows a regular pattern, vanishing practically at every other layer, when N_z is odd, whereas in Fig. 2, it is concave shaped (case of N_z even).

This even-odd feature appears more clearly in the behavior of the finite-size energy gap (see Fig. 5). On the (red) line

$m_0/m_{2\parallel} = -1$ of the phase diagram (Fig. 1), slightly below [WTI-A: (0,100)] and above [STI: (1,000)] the phase boundary at $m_{2\perp}/m_0 = -1/4$ the gap is plotted as a function N_z (the number of stacking layers). In the WTI case: $m_{2z}/m_{2\parallel} = 0.2$, $E_0 = E_0(N_z)$ shows an even/odd feature, and for N_z even, the gap scales as $\sim(N_z + 1)^{-1}$. In the STI case: $m_{2z}/m_{2\parallel} = 0.3$, a weak even/odd feature for small N_z is washed out as N_z increases, and the gap scales as $\sim(N_z + N_x)^{-1}$. In a sense, depending on the parity of the number of stacked layers, the system becomes either trivial (gapped, when N_z even) or gapless (when N_z odd). Physically, this even/odd feature stems from the fact that WTI can be viewed as stacked layers of 2D quantum spin Hall states (here, stacked in the z direction).

B. Effective surface $k \cdot p$ theory

A single Dirac cone cannot be confined (cf. Klein tunneling). This applies to the STI phase we have considered in Sec. III, in which any surface state, instead of being terminated at the end of a plane, continues to the adjacent ones, covering the entire surface. In the WTI phase, typically two Dirac cones appear on its surfaces, i.e., there are "valleys." In that case, one can confine them in a finite area of the surface. Let us sketch explicitly how this is possible.

A typical situation we focus on below is the case in which two side faces of the prism are normal to the weak vector $\vec{v}$, implying that there is no Dirac cone on these surfaces. In such
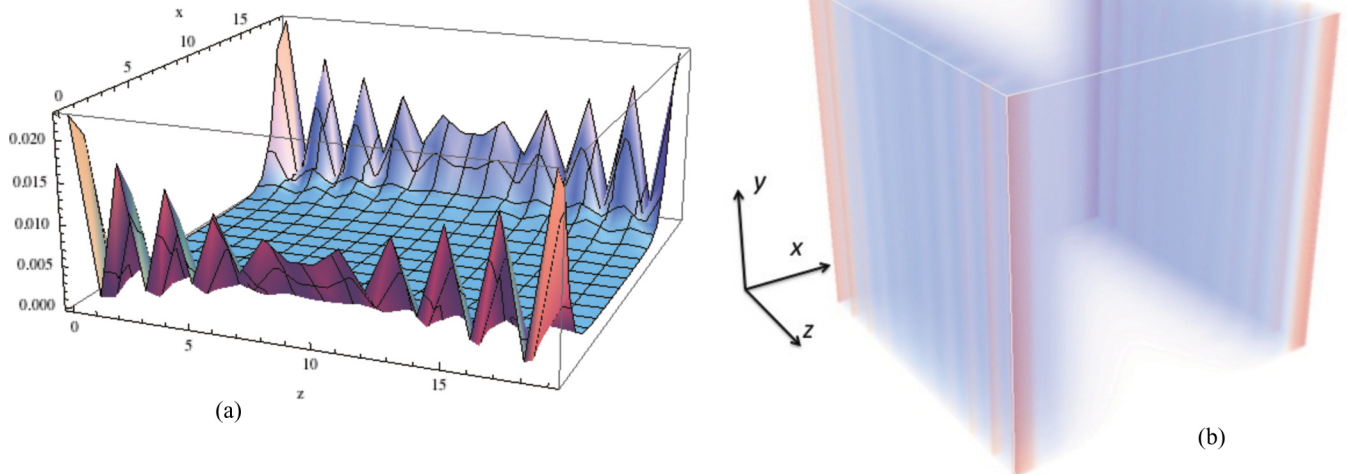

(a)

(b)

FIG. 2. (Color online) Surface wave function in the rectangular prism geometry [Eq. (24)]; WTI phase ($m_{2z}/m_{2\parallel} = 0.2$) with N_z even. (a) The square of the wave function, $|\psi(z,x)|^2$, with $N_z = 20$, $N_x = 20$, and $k_y = 0$ plotted in the (z,x) plane. Spin and orbital indices are summed over; $A_\perp = A_\parallel = 1$. (b) $|\psi(x,y,z)|^2$ is plotted in the 3D (x,y,z) space. The front, upper, and right surfaces correspond, respectively, to the ones normal to $(-1,0,0)$, $(0,1,0)$, and $(0,0,1)$. Fixed boundary condition (FBC) in the z and x directions. PBC in the y direction.
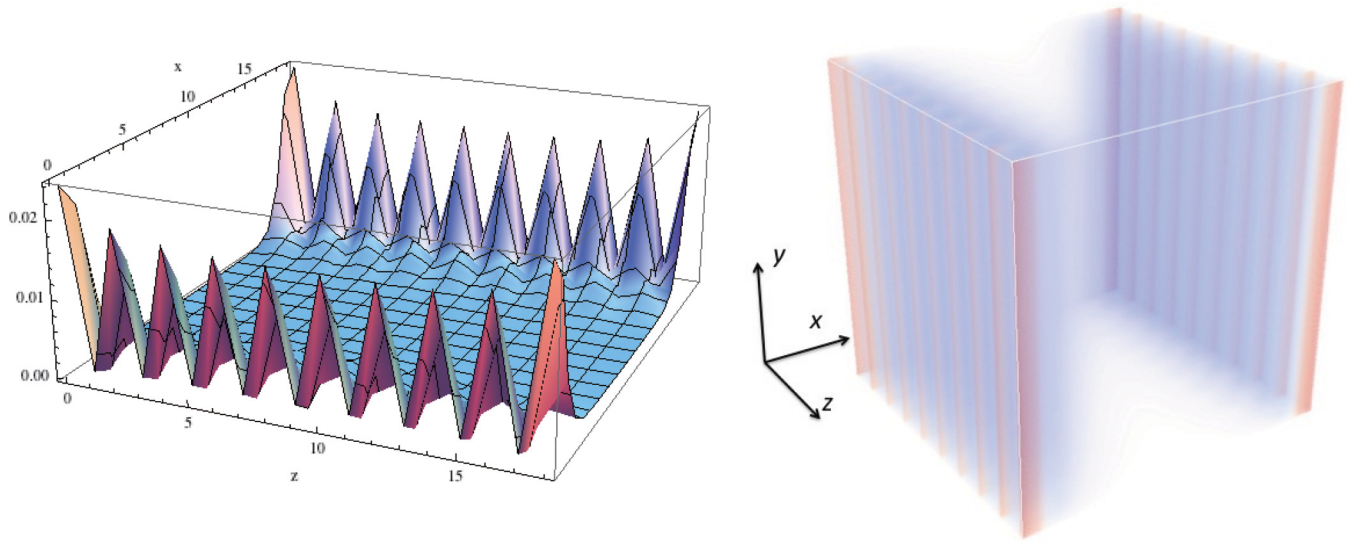
FIG. 3. (Color online) Plots of the surface wave function in the rectangular-prism geometry analogous to Fig. 2. Case of N_z odd ($N_z = 19$). WTI phase. $N_x = 20$, $k_y = 0$, $A_\perp = A_\parallel = 1$. FBC in the z and x directions. PBC in the y direction.

a situation, the wave function of the WTI surface state has a finite amplitude only on the remaining two surfaces parallel to $\vec{\nu}$, and barely penetrates into the side normal to $\vec{\nu}$. The key observation here is that the latter can be regarded as a "boundary condition" for the wave function that lives mainly on the primary parallel surfaces.

Let us consider a simple and concrete example. In the WTI-A phase, shown in Fig. 1, only two $\hat{x}$ surfaces are compatible with the presence of gapless Dirac cones; the remaining $\hat{z}$ surfaces are normal to $\vec{\nu} = (0,0,1)$. We consider the reciprocal space of a $\hat{x}$ surface, spanned by k_y and k_z; here, we tentatively disregard the presence of $\hat{z}$ surfaces, pretending as if the translational symmetry in the z direction is still present. Then, on this $\boldsymbol{k} = (k_y, k_z)$ plane, two Dirac points appear in the spectrum at $\boldsymbol{k}_1 = (0,0)$ and $\boldsymbol{k}_2 = (0,\pi)$. The spectrum of the

rectangular prism is obtained, in a crude approximation, by projecting $E = E(k_y, k_z)$ in the (k_y, k_z) plane onto the k_y axis. When two Dirac cones are superposed in this projection, a more careful treatment on the boundary condition at the corner to the $\hat{z}$ surfaces is needed (see below).

The $\hat{x}$ plane on which we focus is bounded by the $\hat{z}$ surfaces. Penetration of a surface state into the $\hat{z}$ sides is incompatible with the weak vector, $\vec{\nu} = (0,0,1)$. This may be described by a boundary condition on the surface wave function $\psi(y,z)$ on the $\hat{z}$ side,

$$\psi(y, z = 0) = 0, \quad \psi(y, z = N_z + 1) = 0. \quad (26)$$

In the $\boldsymbol{k} \cdot \boldsymbol{p}$ approximation, the wave function $\psi(y,z)$ can be constructed by superposing contributions from one valley surrounding a Dirac point at $\boldsymbol{k}_1$ and another located at $\boldsymbol{k}_2$.
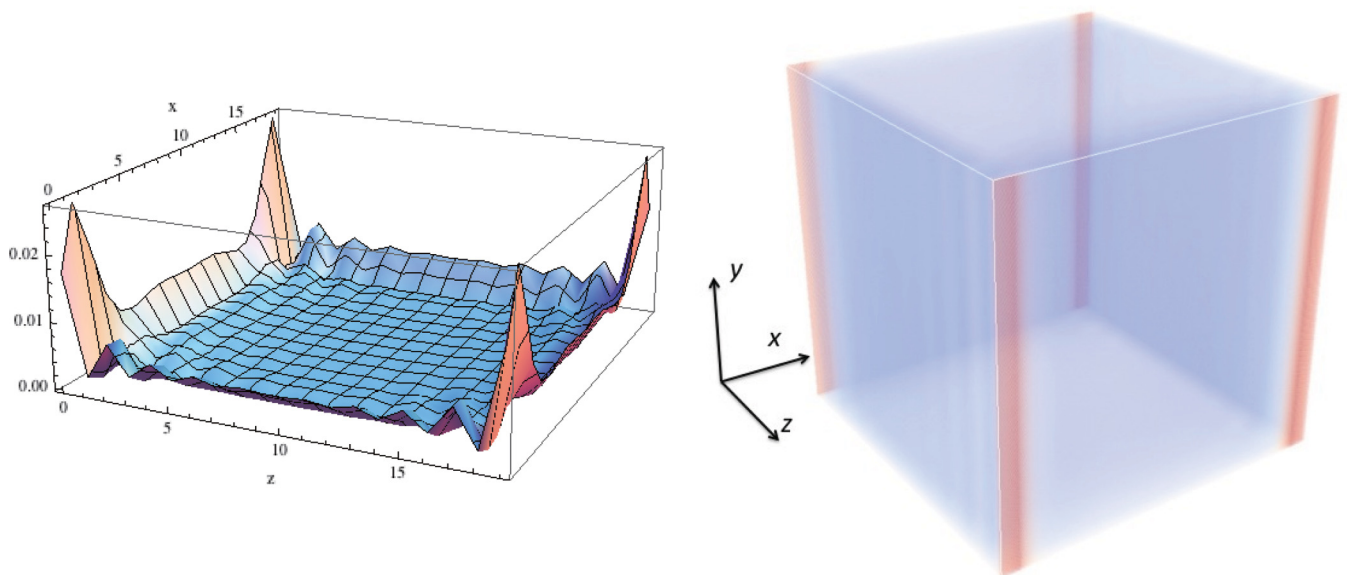

FIG. 4. (Color online) Plots of the surface wave function in the STI case ($m_{2z}/m_{2\parallel} = 0.3$); plots similar to Figs. 2 and 3. Here, the surface wave function is extended over all four facets of the prism.
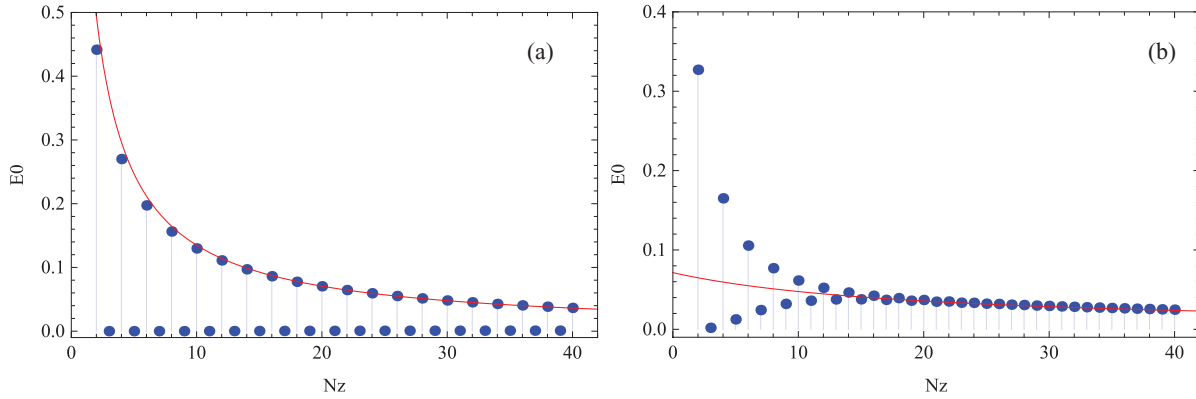
FIG. 5. (Color online) Even/odd feature in the finite-size energy gap (case of WTI). The mass parameters are on the (red) line $m_0/m_{2\perp} = -1$ of the phase diagram (Fig. 1), (a) slightly below (WTI-A case) and (b) above (STI case) the phase boundary at $m_{2\parallel}/m_{2\perp} = 1/4$. The gap is plotted as a function N_z. (a) In the WTI-A case: $m_{2z}/m_{2\parallel} = 0.2$, $E_0 = E_0(N_z)$ shows an even/odd feature, and for N_z, even the gap scales as $\sim (N_z + 1)^{-1}$. (b) In the STI case: $m_{2\perp}/m_{2\parallel} = 0.3$, a weak even/odd feature for small N_z is washed out as N_z increases, and the gap scales as $\sim (N_z + N_x)^{-1}$. $N_x = 20$. $A_\perp = A_\parallel = 1$.

As our system is translationally invariant in the y direction, $\psi(y,z)$ is expressed in the form of

$$\psi(y,z) = e^{ik_y y} \chi(z), \tag{27}$$

where $\chi(z)$ should be chosen to satisfy the boundary conditions (26). This is allowed only when the y components of $\boldsymbol{k}_1$ and $\boldsymbol{k}_2$ are identical as $\boldsymbol{k}_1 = (k_0, k_1)$ and $\boldsymbol{k}_2 = (k_0, k_2)$. This is indeed the case in the WTI-A phase, where $k_0 = 0$, $k_1 = 0$, and $k_2 = \pi$. The superposition yields

$$\chi(z) = e^{i(k_1 + p_1)z} - e^{i(k_2 + p_2)z}, \tag{28}$$

where p_1 and p_2 are small displacements from the corresponding Dirac points. Note that this automatically satisfies the boundary condition at $z = 0$. If $\chi(z)$ with $p_1 = p_2 = 0$ (i.e., the superposition of the wave functions just at the two Dirac points) is compatible with the other boundary condition at $z = N_z + 1$, then the resulting wave function has the zero-energy eigenvalue at $k_y = k_0$, resulting in the gapless surface states. This occurs typically at N_z *odd*, and in the WTI-A phase with $k_1 = 0$ and $k_2 = \pi$. Contrastingly, if finite displacements (i.e., $p_1, p_2 \neq 0$) are necessary to satisfy the boundary condition, then a finite-size gap inevitably appears. Naturally, the latter applies to the case of N_z *even*. These two contrasting behaviors explain the nature of the even/odd feature demonstrated in Fig. 5.

Let us further quantify the case of N_z even. To fulfill the requirement of Eq. (26), we set $p_1 = -p_2 = q$. The boundary condition at $z = N_z + 1$ is satisfied, if

$$q = \pm \frac{n}{2(N_z + 1)} \pi, \tag{29}$$

and n is an odd integer. The lowest-energy solution with $n = 1$ determines the energy gap to be

$$E_0 = \frac{A}{2(N_z + 1)} \pi, \tag{30}$$

i.e., E_0 scales as $(N_z + 1)^{-1}$ for N_z even within the range of validity of the $\boldsymbol{k} \cdot \boldsymbol{p}$ approximation. Equation (30) allows for comparing the above simple effective theory with the calculated spectrum. This is done in Fig. 5 by plotting

the energy gap obtained by numerical diagonalization of the corresponding tight-binding model against the postulated scaling of Eq. (30).

A similar comparison can be made for the shape of the surface wave function. Plugging Eq. (29) with $n = 1$ back into Eq. (28), one finds

$$|\chi(z)|^2 = 4 \sin^2 \left[\frac{N_z \pi}{2(N_z + 1)} z \right]. \tag{31}$$

The shape of this envelop function is to be compared with the calculated value of the amplitude of the surface-state eigenspinor at $x = 1$, which is shown in Fig. 6.

It is suggestive to apply the above $\boldsymbol{k} \cdot \boldsymbol{p}$ effective theory to the case of WTI-B and WTI-C phases (see Fig. 1). These two topologically different WTI phases appear on the blue line $m_0/m_{2\parallel} = -5$ in the phase diagram with the phase boundary at $m_{2\perp}/m_{2\parallel} = -1/4$. The crossover of the finite-size energy gap at the transition between these two WTI phases is precisely
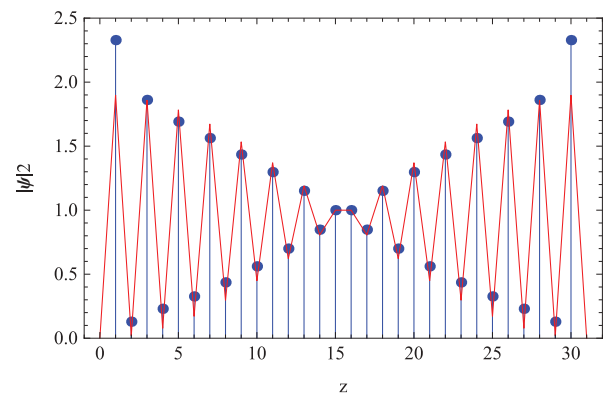

FIG. 6. (Color online) Shape of the surface wave function: tight-binding model vs $\boldsymbol{k} \cdot \boldsymbol{p}$ approximation. $|\psi(z)|^2$, the squared amplitude of the surface state wave function at $x = 1$ (and in the case of $k_z = 0$), is plotted for the case of N_z even ($N_z = 30$, blue points). A continuous red curve is the prediction of $\boldsymbol{k} \cdot \boldsymbol{p}$ theory [cf. Eq. (31)]. As in Fig. 2, the mass parameters are chosen to be $m_0/m_{2\parallel} = -1$, $m_{2\perp}/m_{2\parallel} = 0.2$; other parameters are also set as in Fig. 2.
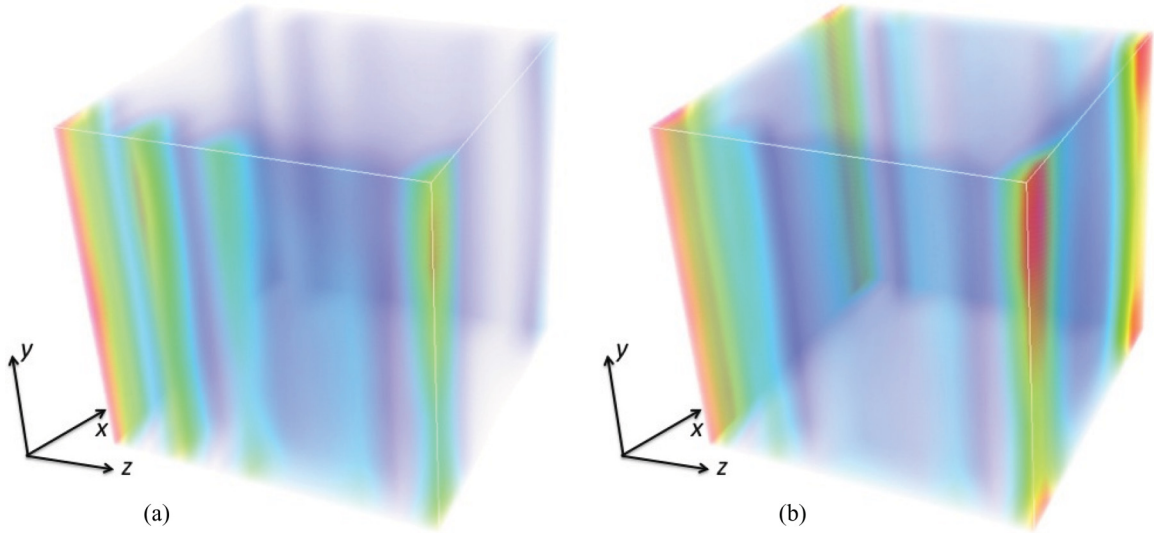
FIG. 7. (Color online) Surface wave function in the presence of disorder. Comparison of the WTI and STI cases: (a) $m_{2z}/m_{2\parallel} = 0.2$ vs (b) $m_{2z}/m_{2\parallel} = 0.3$. Here, the simulation is done for a system of size $N_x \times N_y \times N_z = 10 \times 10 \times 10$; i.e., N_z is even.

in parallel with the one between the STI and WTI-A phases (on the red line: $m_0/m_{2\parallel} = -1$ in Fig. 1) that we have considered so far. In the case of the WTI-B and WTI-C phases, the constituent surface Dirac cones on the $\boldsymbol{k} = (k_y, k_z)$ plane appear at $\boldsymbol{k}_1 = (\pi, 0)$ and $\boldsymbol{k}_2 = (0, \pi)$ in the WTI-B phase, and at $\boldsymbol{k}_1 = (\pi, 0)$ and $\boldsymbol{k}_2 = (\pi, \pi)$ in the WTI-C phase. Here, the relative position of the two Dirac cone is essential. In the case of the WTI-C phase, one can construct the surface wave function (28) compatible with the specific boundary condition (26) precisely in parallel with the previous case of the WTI-A phase, simply by replacing $k_0 = 0$ with $k_0 = \pi$, leading to the same even/odd feature. Notice that the surface Dirac cone in the WTI-C phase appears in the spectrum of prism geometry, $E = E_{\mathrm{prism}}(k_y)$ at $k_y = \pi$.

In the case of the WTI-B phase, the two Dirac cones at $\boldsymbol{k}_1 = (\pi, 0)$ and $\boldsymbol{k}_2 = (0, \pi)$ are projected onto a different point on the k_y axis, making the previous construction [Eqs. (27) and (28)] impossible. This is, of course, consistent with the fact that in the WTI-B phase, the surface states are not confined to the $\hat{\boldsymbol{x}}$ surfaces. This observation, in turn, reveals that the relative orientation of the two (even number of) Dirac cones in the WTI is indeed imposed by the weak indices. On surfaces parallel to the weak vector $\vec{\nu}$, they must appear in line in the direction of $\vec{\nu}$.

C. Effects of disorder

Let us comment here on the robustness of the surface states discussed in the previous sections against disorder. A motivation for this is that since disorder leads generally to repulsion of the energy levels, one naturally questions whether the finite-size effects discussed so far are still meaningful when the size gap is perturbed by the effects of level repulsion by disorder. The effects of disorder are taken into account by introducing a random potential $V(\boldsymbol{r})$, which obeys a uniform distribution in the period $[-W/2, W/2]$ at each site $\boldsymbol{r}$ of the cubic lattice, i.e., a scalar random potential, $\propto \mathbf{1}$ in the real and

orbital spin space, which is also cite diagonal:

$$V = \sum_{\boldsymbol{r}} V(\boldsymbol{r})\mathbf{1} \otimes |\boldsymbol{r}\rangle\langle\boldsymbol{r}|, \quad V(\boldsymbol{r}) \in [-W/2, W/2] \quad (32)$$

is added to the tight-binding Hamiltonian (1) represented in the real space. In Eq. (32), the summation over $\boldsymbol{r}$ should be taken over all the lattice sites on the cubic lattice, $\boldsymbol{r} = (x, y, z)$ with $x = 1, 2, \ldots, N_x, y = 1, 2, \ldots, N_y$, and $z = 1, 2, \ldots, N_z$. In the actual computation, we set $W = 1, m_0 = -1, A_\perp = A_\parallel = 1$ in units of $m_{2\parallel}$ (which is set to be unity).

In Fig. 7, plots similar to Figs. 2–4 performed in the presence of disorder are shown. In Fig. 7(a) (WTI case), the surface wave function is localized mainly on one facet of the prism. This is in contrast to the clean cases (Figs. 2 and 3) and to the STI case [Fig. 7(b)], in which the surface state is extended over all four facets of the prism. The stripe-shaped structure is also still visible, indicating that the surface wave functions of a specific shape discussed in the previous section possess some robustness against disorder.

D. STI more gapped than WTI

We finally discuss the N_x dependence of the size gap. As shown in Table II, there are three different types of behaviors in the N_x dependence of the size gap, each corresponding to the three different gap-opening mechanisms we have highlighted in this paper. Here, let us focus again (cf. Fig. 5) on the (red) line $m_0/m_{2\parallel} = -1$ in the phase diagram (Fig. 1) slightly above and below the phase boundary at $m_{2\perp}/m_0 = -1/4$, and compare the STI: (1,000) and WTI-A: (0,001) phases. In the following demonstrations (Figs. 8–10), however, we use a slightly different set of parameters inspired by the corresponding material parameters of Bi_2Se_3,[21] but focus on the same phase boundary between STI and WTI-A. Here, the tight-binding parameters are specially adjusted[34] to reproduce the band structure in the vicinity of the Z point obtained by the first-principles calculation. The employed
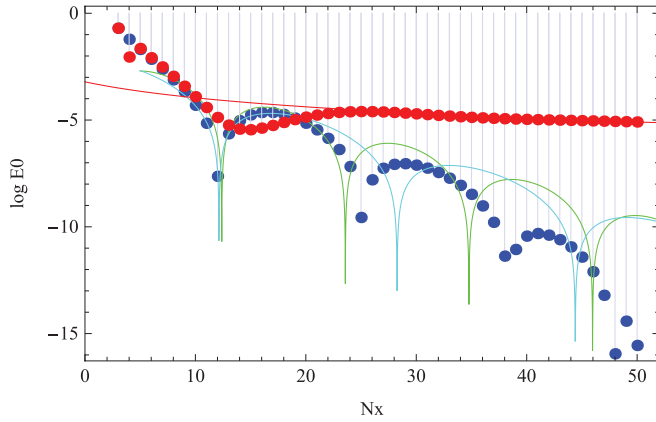
FIG. 8. (Color online) Finite-size energy gap in the rectangular-prism geometry plotted as a function of the "width" N_x. Comparison between the WTI (blue points) and STI (red points) regimes in the case of prism thickness N_z odd ($N_z = 9$). The logarithm of the energy gap E_0 is plotted vs N_x for demonstrating that $E_0 = E_0(N_x)$ decays exponentially, showing actually an exponentially damped oscillation in the WTI phase. The corresponding solutions of Eq. (B10) are a pair of complex numbers (see main text for details). The model parameters employed are also given there.

parameters are given explicitly as

$$m_0 = -0.1, \quad m_{2z} \equiv m_{2\perp} = 0.1, \quad m_{2\parallel} = 1,$$
$$A_z \equiv A_\perp = 0.1, \quad A_\parallel = 0.3. \tag{33}$$

Here, the parameters are normalized in units of $m_{2\parallel} \simeq 2.60$ eV. This set of parameters corresponds to the case of the STI phase. To achieve a weak phase, we modify the value of $m_{2\perp}$ in Eq. (33) as $m_{2\perp} \to 0.01$. This indeed falls on the WTI-A phase in Fig. 1. The spectrum of the *strong* phase is "gapped," showing a finite-size energy gap due to spin-to-surface locking, which decays only algebraically, $E_0 \sim (N_z + N_x)^{-1} \neq 0$. In the *weak* phase, and in the case of N_z odd considered here, the spectrum is "gapless," decaying exponentially as a function of the distance $\sim N_x$ between the two *ideally* gapless patches ($\log E_0 \propto -N_x$, $E_0 \simeq 0$). This is indeed a comparison of the
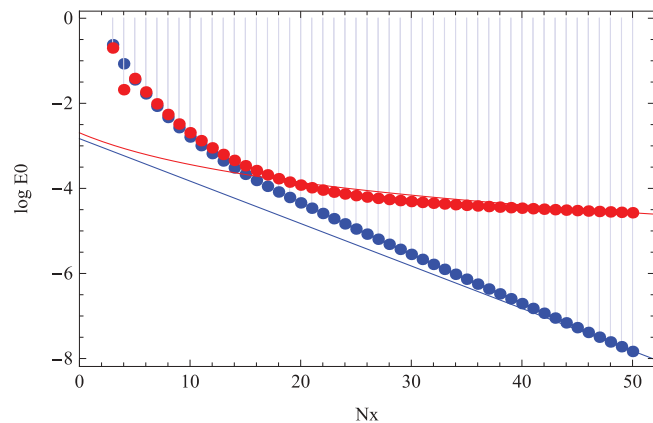

FIG. 9. (Color online) Size dependence of $E_0 = E_0(N_x)$ in the case of N_z odd ($N_z = 9$). A plot similar to Fig. 8, but in the case of model parameters, yielding, as solutions for ρ in Eq. (B10), two real solutions given in the main text. The data points for the WTI and STI cases are shown, respectively, in blue and red.
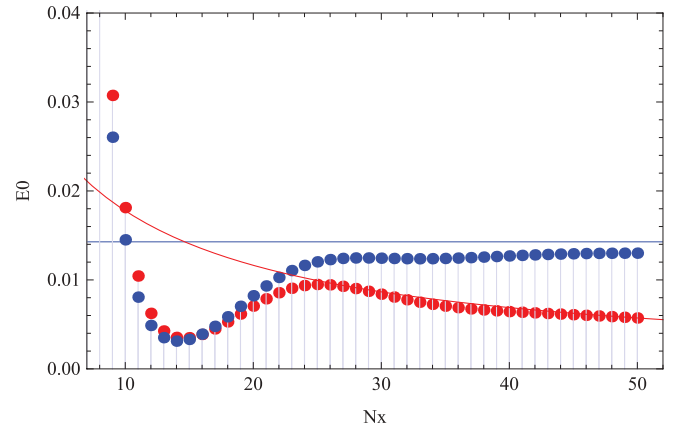

FIG. 10. (Color online) Size dependence of $E_0 = E_0(N_x)$ in the case of N_z even ($N_z = 10$). The mass and velocity parameters are chosen to be the same as in the case of Fig. 8. Here, the vertical axis for E_0 is in the linear scale. For N_z even, $E_0(N_x)$ shows at most a power-law decay, whether the system is in the STI or WTI phase (see Table II). The data points for the WTI and STI cases are as shown before, respectively, as blue and red filled circles.

cases (ii) and (iii) in Table II. In Fig. 8, the logarithm of the energy gap E_0 is plotted vs N_x, taking into account such an expected exponential decay in the WTI-A phase. But here, a systematic deviation from a simple exponential decay can be clearly seen, implying that this is rather a damped oscillation.

As mentioned in Appendix B, the magnitude of the finite-size energy gap in the slab is directly related to the (complex) penetration depth of the surface wave function, or $\rho_{1,2}$ given in Eq. (B10). One can indeed verify

$$E_0(N_x) \propto \left| \rho_1^{N_x+1} - \rho_2^{N_x+1} \right|. \tag{34}$$

Recall that in the WTI-A phase considered here, two Dirac cones, one at $\boldsymbol{k}_1 = (0,0)$ and the other at $\boldsymbol{k}_2 = (0,\pi)$, are well grounded on the $\hat{\boldsymbol{x}}$ surfaces. The corresponding surface wave functions exhibit different penetration depths at each Dirac point, which are specified by Eq. (B10). The solutions of Eq. (B10) at $\boldsymbol{k}_1 = (0,0)$ are

$$\rho = \rho_{1,2}(\boldsymbol{k}_1) \simeq 0.826 \pm 0.238\, i, \tag{35}$$

while they are given by

$$\rho = \rho_{1,2}(\boldsymbol{k}_2) \simeq 0.843 \pm 0.166\, i, \tag{36}$$

at $\boldsymbol{k}_2 = (0,\pi)$, i.e., in the two cases, they become a pair of complex numbers. In the slab, the finite-size energy gap is $\boldsymbol{k} = (k_z, k_x)$ resolved; $E_0 = E_0(\boldsymbol{k})$, simply the minimal value of which determines the actual magnitude of the finite-size energy gap. In the case of a rectangular prism, contributions from $\boldsymbol{k} = \boldsymbol{k}_1$ and $\boldsymbol{k} = \boldsymbol{k}_2$ are superposed to cope with the boundary condition. Notice also that here the surface wave functions at $\boldsymbol{k} = \boldsymbol{k}_1$ and $\boldsymbol{k} = \boldsymbol{k}_2$ are both oscillatory [Eqs. (35) and (36)]. These two features combine to give the oscillatory pattern of $\log E_0$ in the WTI case in Fig. 8. In the figure, two "theoretical" curves for $\log E_0$ are shown in solid curves for comparison, not showing a quantitative agreement with the actual data. The two curves correspond to the finite-size energy gap given as in Eq. (34) at $\boldsymbol{k} = \boldsymbol{k}_1$ (green) and $\boldsymbol{k} = \boldsymbol{k}_2$ (cyan), which are

estimated under the hypothesis that the system is slab shaped. The actual N_x dependence of $\log E_0$ is somewhere in between.

Figure 9 is a plot similar to Fig. 8, making the same comparison of the STI and WTI-A phases for the same N_z odd case, except that the model parameters are slightly modified from Eq. (33). We replace one of the velocity parameters $A_{2\parallel}$ with $A_{2x} = 0.7$, leaving $A_{2y} = 0.3$ (the same value as before). This replacement makes the corresponding solutions of Eq. (B10) two real solutions, indicating that the surface wave function exhibits a simple exponential decay. In the WTI-A phase, we have chosen, as before, $m_{2\perp} = 0.01$. The behavior of $\log E_0$ in the WTI case is qualitatively different from the previous case. At the two Dirac points, $\boldsymbol{k} = \boldsymbol{k}_1$ and $\boldsymbol{k} = \boldsymbol{k}_2$, in the WTI phase, the solutions of Eq. (B10) are

$$\rho_1(\boldsymbol{k}_1) \simeq 0.821, \quad \rho_2(\boldsymbol{k}_1) \simeq 0.587, \tag{37}$$

at $\boldsymbol{k}_1 = (0,0)$, while they are given by

$$\rho_1(\boldsymbol{k}_2) \simeq 0.905, \quad \rho_2(\boldsymbol{k}_2) \simeq 0.532, \tag{38}$$

at $\boldsymbol{k}_2 = (0,\pi)$. The actual magnitude of the size gap is determined by the largest value of $\rho_{1,2}$, which is the value of ρ_1 at $\boldsymbol{k} = \boldsymbol{k}_2$. Indeed, the actual N_x dependence of $\log E_0$ approaches to this scaling behavior [$E_0 \propto \rho_1(\boldsymbol{k}_2)^{N_x}$, shown in a solid straight line in Fig. 9] for large enough N_x.

Through these two examples, we can convince ourselves that in this configuration imposed by the combination of the prism geometry and a specific choice of the weak vector, which can be achieved by adjusting the crystal growth direction with respect to the prism, the strong topological insulator is qualitatively more gapped than a weak topological insulator.

In Fig. 10, we make a comparison between the cases (i) and (iii) in Table II, in contrast to the previous plots, i.e., the ones in Figs. 8 and 9. The model parameters are the same as in Fig. 8, but here the number N_z of stacking layers is even ($N_z = 10$). In the STI case, the size gap shows a power-law decay, $E_0 \sim (N_z + N_x)^{-1} \neq 0$, due to spin-to-surface locking. In the WTI-A phase, the size gap implied by Eq. (30) does not scale as a function of N_x, but is given simply by

$$E_0 = \frac{A_z}{2(N_z + 1)}\pi = 0.1 \times \frac{\pi}{22}. \tag{39}$$

In Fig. 10, this value is indicated as a horizontal grid line (in blue). For sufficiently large value of N_x, the data looks almost constant at a value not far from the one of Eq. (39).

We have seen so far that from the viewpoint of the scaling behavior of a finite-size energy gap, *the statue of the strong and weak phases could be reversed*. Here, to illustrate this feature, we have considered only a very representative range of parameters, but the same feature is generic to the vicinity of transitions between the STI and WTI phases with a suitable choice of the surface directions and the number of quintuple layers.

V. CONCLUSIONS

We have studied the finite-size energy gap in 3D weak and strong topological insulators. Employing the standard Wilson-Dirac-type effective model, we have developed both numerical and analytical considerations. It has been demonstrated that anisotropy of the model and the geometry of the system are among other model parameters crucial elements for

determining the qualitative nature of the finite-size energy gap. The two elements manifest in a correlated manner. The weak topological insulator (WTI) has a specific property of (i) expelling the gapless surface state from surfaces normal to its weak vector $\vec{\nu}$ ($\simeq$ weak indices), i.e., no Dirac cone on the surface normal to $\vec{\nu}$, but (ii) on surfaces parallel to the weak vector, it bears two Dirac cones [more Dirac cones than a strong topological insulator (STI)]. We have seen in this paper through the study of finite-size effects that these two, seemingly competing, characteristics of the WTI operate, in fact, in a cooperative way (cf. the $\boldsymbol{k} \cdot \boldsymbol{p}$ description of the surface state in the WTI phase; Sec. IV B). The condition of no Dirac cone on the side normal to $\vec{\nu}$ imposes the relative orientation of the two Dirac cones on the side parallel to $\vec{\nu}$. The weak indices are also much related to the anisotropy of the model parameters. To encompass different scaling behaviors of the finite-size energy gap, we have manipulated the weak indices by varying the model parameters, guided by the phase diagram shown in Fig. 1.

Spin-to-surface locking is a characteristic feature of the topological insulator surface state, operational both in the WTI and STI phases, leading also to a finite-size energy gap that exhibits a specific power-law decay as a function of the system's linear dimension. Clearly, this is more relevant than a usual exponential decay associated with the overlap of two surface wave functions, e.g., sitting on the opposing sides of the slab geometry. By its nature, the finite-size energy gap due to spin-to-surface locking is not effective in the slab, but is effective in the prism-shaped geometry. In the prism-shaped WTI samples, the interplay of these three ingredients, i.e., the weak vector, the spin-to-surface locking, and the rectangular-prism geometry, leads to intricate finite-size effects, depending on the model parameters. Three different gap-opening mechanisms pointed out in this paper, i.e., mixing of the surface wave functions [case (ii) in Table II], spin-to-surface locking [case (iii) in Table II], and commensurability with the boundary condition [case (i) in Table II], are all effective in determining the intricate size dependence of the energy gap in the rectangular-prism geometry.

APPENDIX A: TOPOLOGICAL NUMBERS

Notice that our model specified by Eqs. (1) and (2) has inversion symmetry. This allows us to find the strong and weak $\mathbb{Z}_2$ indices with the use of Fu-Kane's formula.[23] Here, we mention that in the specific case of $\epsilon(\boldsymbol{k}) = 0$ (in most of the analyses in this paper, we employ this condition for mathematical simplicity), one can introduce a $\mathbb{Z}$-type winding number N_3. The strong index ν_0 is related to N_3 as $\nu_0 = N_3 \bmod 2$.
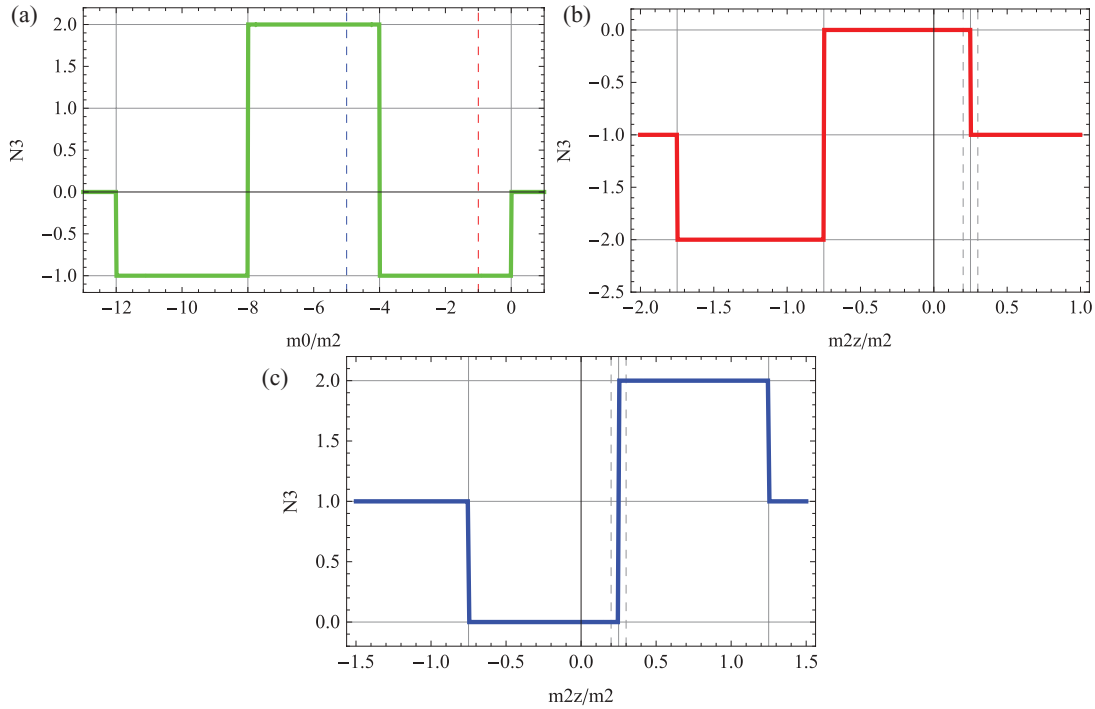
FIG. 11. (Color online) The winding number N_3 [given in Eq. (A4)], evaluated on a horizontal or vertical line in Fig. 1. In (a), $m_{2\perp}/m_{2\parallel}$ is fixed at the isotropic point ($m_{2\perp}/m_{2\parallel} = 1$), with $m_0/m_{2\parallel}$ being varied, while in the remaining panels, $m_0/m_{2\parallel}$ is fixed (b) at $m_0/m_{2\parallel} = -1$ and (c) at $m_0/m_{2\parallel} = -5$ with $m_{2\perp}/m_{2\parallel}$ being varied. The lines are shown in the same color in the phase diagram (see Fig. 1).

In terms of the periodic table,[15,35–39] our starting bulk effective Hamiltonian (1) falls on the class AII. This class of models has the symmetry $\Theta^2 = -1$, $\mathcal{C}^2 = 0$, and $\Gamma_5 = 0$, where Θ, $\mathcal{C}$, and Γ_5 represent, respectively, the time-reversal, particle-hole, and chiral symmetries, and in this terminology "0" indicates that the system does not possess that type of symmetry. The periodic table says that class AII models are characterized by $\mathbb{Z}_2$-type bulk topological invariants in 3D. For the specific case of $\epsilon(\mathbf{k}) = 0$ in our model, the symmetry of the model is upgraded to the class DIII, i.e., $\Theta^2 = -1$, $\mathcal{C}^2 = 1$, and $\Gamma_5 = 1$, where for the specific Hamiltonian, given by Eq. (1), $\mathcal{C}$ and Γ_5 are given by $\mathcal{C} = \sigma_y \tau_y K$ and $\Gamma_5 = \tau_y$. This symmetry class allows for the $\mathbb{Z}$-type bulk topological classification in 3D, characterized by a $\mathbb{Z}$-type winding number N_3, to be defined below.

To construct the winding number N_3 explicitly, let us first represent the bulk Hamiltonian (1), using an explicit matrix representation for the orbital Pauli matrices τ_x and τ_y as

$$H_{\text{bulk}} = \begin{bmatrix} 0 & m(\mathbf{k}) - i P_\mu(\mathbf{k})\sigma_\mu \\ m(\mathbf{k}) + i P_\mu(\mathbf{k})\sigma_\mu & 0 \end{bmatrix}, \quad (A1)$$

where we have introduced $P_\mu(\mathbf{k}) = A_\mu \sin k_\mu$. Dividing the Hamiltonian by (the magnitude of) its own eigenvalue $E(\mathbf{k})$, one can also flatten the spectrum of the Hamiltonian as

$$\widetilde{H}(\mathbf{k}) = \frac{H_{\text{bulk}}(\mathbf{k})}{|E(\mathbf{k})|} = \begin{bmatrix} 0 & Q(\mathbf{k}) \\ Q^\dagger(\mathbf{k}) & 0 \end{bmatrix}, \quad (A2)$$

where $E(\mathbf{k}) = \pm\sqrt{m(\mathbf{k})^2 + P_\mu(\mathbf{k})^2}$, and

$$Q(\mathbf{k}) = \frac{m(\mathbf{k}) - i P_\mu(\mathbf{k})\sigma_\mu}{|E(\mathbf{k})|}. \quad (A3)$$

Note that the matrix Q defined above is a 2×2 $\mathbb{SU}(2)$ matrix, satisfying $Q^\dagger Q = \mathbf{1}$ and $\det Q = 1$. Then, one can introduce an integral winding number N_3,[40–42] characterizing the mapping of the 3D Brillouin zone onto this $\mathbb{SU}(2)$ matrix as

$$N_3 = \frac{1}{24\pi^2} \int_{\text{BZ}} d^3k \, \epsilon_{\mu\nu\lambda} \text{Tr}[\Gamma_\mu \Gamma_\nu \Gamma_\lambda], \quad (A4)$$

where $\Gamma_\mu = Q^\dagger \partial_{k_\mu} Q$. The integration should be done over the entire 3D Brillouin zone. We have evaluated this winding number numerically over the entire range of parameters shown in Fig. 1 to verify that

$$\nu_0 = N_3 \bmod 2 \quad (A5)$$

indeed holds. The explicit values of N_3 in the different STI and WTI phases are also shown in Fig. 1. The same calculated value is also shown continuously in Fig. 11 as a function of a control parameter, either $m_0/m_{2\parallel}$ or $m_{2\perp}/m_{2\parallel}$, on a few specific lines in Fig. 1.

APPENDIX B: PENETRATION OF THE SURFACE WAVE FUNCTION IN THE SLAB GEOMETRY

To quantify the surface electronic state in the slab geometry, let us concentrate on one surface of the slab. Also, we choose this flat surface normal to the $\hat{x}$ direction. To find the wave function which is localized in the vicinity of the surface, we divide the bulk Hamiltonian (1) into two parts:

$$H_{\text{bulk}}(\mathbf{k}) = H_\parallel(\mathbf{k}_\parallel) + H_\perp(k_x), \quad (B1)$$

where $\mathbf{k}_\parallel = (k_y, k_z)$, and

$$H_\parallel(\mathbf{k}_\parallel) = \tau_x m_\parallel(\mathbf{k}_\parallel) + \tau_y(\sigma_y A_y \sin k_y + \sigma_z A_z \sin k_z), \quad (B2)$$

with $m_\parallel(\boldsymbol{k}_\parallel)$ defined as

$$m_\parallel(\boldsymbol{k}) = m_0 + 2m_{2x} + 2m_{2y}(1 - \cos k_y) + 2m_{2z}(1 - \cos k_z),$$

(B3)

and

$$H_\perp(k_x) = -2\tau_x m_{2x} \cos k_x + \tau_y \sigma_x A_x \sin k_x. \quad (B4)$$

This and the following procedure are in parallel with the case in which we deal with the continuum model, a more standard situation in the context of a $\boldsymbol{k} \cdot \boldsymbol{p}$ approximation, discussed in Appendix C, but here we solve the lattice model directly without taking the continuum limit.[43,44] Physically, the decomposition (B1) is based on the picture that each (y,z) plane described by $H_\parallel(\boldsymbol{k}_\parallel)$ is coupled by $H_\perp(k_x)$ to the neighboring layers. In the present geometry, $\boldsymbol{k}_\parallel = (k_y, k_z)$ is a good quantum number. Here, we assume that the system is extended in the half space, $x \geqslant 1$, and impose a boundary condition, $\psi(x = 0) = 0$. A surface solution in such a geometry can be constructed by composing a linear combination of base solutions of the form $\psi(x) = \rho^x \psi_0$ $(|\rho| < 1)$. For such damped (instead of plane-wave) solutions, Eq. (B4) modifies to

$$H_\perp(\rho) = -2\tau_x m_{2x} \frac{\rho + \rho^{-1}}{2} + \tau_y \sigma_x A_x \frac{\rho - \rho^{-1}}{2i}. \quad (B5)$$

In the surface energy spectrum $E = E(\boldsymbol{k}_\parallel)$, protected gapless Dirac points can appear at any of the four TRIM: $\boldsymbol{k}_{\mathrm{TRIM}} = (0,0),(\pi,0),(0,\pi),(\pi,\pi)$. At such TRIM of the surface BZ, the hopping terms in $H_\parallel(\boldsymbol{k}_\parallel)$ become inert:

$$H_\parallel(\boldsymbol{k}_\parallel = \boldsymbol{k}_{\mathrm{TRIM}}) = \tau_x m_\parallel(\boldsymbol{k}_{\mathrm{TRIM}}). \quad (B6)$$

This significantly simplifies the derivation of $\psi(\boldsymbol{k}_\parallel)$ at $\boldsymbol{k}_\parallel = \boldsymbol{k}_{\mathrm{TRIM}}$. Notice also that Eq. (B2) with (B3) can be regarded as a lattice Hamiltonian for a 2D $\mathbb{Z}_2$ TI with an effective mass parameter $m_{\mathrm{2D}} = m_0 + 2m_{2x}$. Here, $m_{\mathrm{2D}} < 0$ $(m_{\mathrm{2D}} > 0)$ corresponds, respectively, to the nontrivial $(\nu = 1)$ vs trivial $(\nu = 0)$ phases, where ν is the 2D $\mathbb{Z}_2$ index. A situation described by this couple of equations is realized in the limit $N_x \rightarrow 1$.

Let us construct the surface wave function,

$$\psi(\boldsymbol{k}_\parallel, x) = \rho^x \psi_0(\boldsymbol{k}_\parallel), \quad (B7)$$

explicitly at $\boldsymbol{k}_\parallel = \boldsymbol{k}_{\mathrm{TRIM}}$. At TRIM, $\psi_0(\boldsymbol{k}_\parallel)$ satisfies

$$H_{\mathrm{bulk}}\psi_0 = [\tau_x m_\parallel(\boldsymbol{k}_{\mathrm{TRIM}}) + H_\perp(\rho)]\psi_0 = \boldsymbol{0}, \quad (B8)$$

i.e., ψ_0 is a zero-energy eigenstate of

$$\tau_x H_{\mathrm{bulk}} = m_\parallel(\boldsymbol{k}_{\mathrm{TRIM}}) - m_{2x}(\rho + \rho^{-1}) + \tau_z \sigma_x \frac{A_x}{2}(\rho - \rho^{-1}). \quad (B9)$$

Similarly to the case of the continuum model (see Appendix C), this zero-energy condition is proven to be necessary[40] for constructing a surface solution compatible with the boundary condition at $x = 0$ in the form of Eq. (B12). Clearly, any of the four simultaneous eigenstates of τ_z and σ_x, $\psi_{\pm\pm} = |\tau_z\pm\rangle|\sigma_z\pm\rangle$, is an eigenstate of the reduced operator (B9). Then the zero-energy condition can be used, in

turn, to determine ρ as

$$\rho = \frac{m_\parallel \pm \sqrt{m_\parallel^2 - 4\left(m_{2x}^2 - A_x^2/4\right)}}{2(m_{2x} \pm A_x/2)} \equiv \rho_{1,2}, \quad (B10)$$

where

$$m_\parallel = m_\parallel(\boldsymbol{k}_{\mathrm{TRIM}}) \equiv m_0(\boldsymbol{k}_{\mathrm{TRIM}}) + 2m_{2x}. \quad (B11)$$

Here, $m_0(\boldsymbol{k}_{\mathrm{TRIM}})$ represents the magnitude of the bulk energy gap at $\boldsymbol{k} = \boldsymbol{k}_{\mathrm{TRIM}}$. In Eq. (B10), the meaning of two double signs may need some explanation; the one in the numerator is arbitrary, with each choice corresponding to $\rho_{1,2}$. The one in the denominator represents $+$ for $\psi_0 = \psi_{++}$ and ψ_{--}, whereas, the same sign represents $-$ for $\psi_0 = \psi_{+-}$ and ψ_{-+}. The structure of Eq. (B9) with the understanding that $\tau_z \sigma_x = \pm 1$ indicates that if ρ satisfies the zero-energy condition, then so does ρ^{-1}. With a suitable choice of ψ_0, satisfying both $|\rho_1| < 1$ and $|\rho_2| < 1$, the surface solution can be constructed as

$$\psi(x) = \left(\rho_1^x - \rho_2^x\right)\psi_0. \quad (B12)$$

In a separate paper,[45] we study in detail various aspects of the finite-size effects in a slab-shaped sample. The magnitude of the finite-size energy gap in the slab is determined by the overlap of the two surface wave functions sitting on the opposing sides of the slab. It is, therefore, naturally expected that the magnitude of the gap (in a slab of width N_x) is essentially determined by the penetration depth, or the amplitude of the wave function (B12) at the depth of $x = N_x$. Here, in this model, one can verify that the correlation of theses two quantities is a bit stronger than this. The magnitude of the size energy gap $E_0(N_x)$ is indeed directly proportional to $|\psi(N_x)|$ as given in Eq. (34).

APPENDIX C: DERIVATION OF THE EFFECTIVE SURFACE HAMILTONIAN IN THE CYLINDER GEOMETRY

To find the surface effective Hamiltonian on the cylinder in the spirit of a $\boldsymbol{k} \cdot \boldsymbol{p}$ approximation,[7,11,21] one first divides the bulk 3D effective Hamiltonian (4) into two parts; one is perpendicular and the other is parallel to the cylindrical surface:

$$H = H_\perp(p_r) + H_\parallel(p_\phi, p_z), \quad (C1)$$

where $H_\perp = H|_{p_\phi = p_z = 0}$, and $p_r = -i\partial/\partial r$. $H_\perp$ and $H_\parallel$ read, explicitly,

$$
\begin{aligned}
H_\perp &= m_\perp \tau_x + A p_r \tau_y (\sigma_x \cos \phi + \sigma_y \sin \phi) \\
&= \tau_x [m_\perp + i A p_r \tau_z \hat{\boldsymbol{r}} \cdot \boldsymbol{\sigma}], \quad (C2)
\end{aligned}
$$

$$
\begin{aligned}
H_\parallel &= m_\parallel \tau_x + A\tau_y[p_\phi(-\sin\phi\,\sigma_x + \cos\phi\,\sigma_y) + p_z\sigma_z] \\
&= m_\parallel \tau_x + A\tau_y[p_\phi\hat{\boldsymbol{\phi}} \cdot \boldsymbol{\sigma} + p_z\sigma_z], \quad (C3)
\end{aligned}
$$

where

$$m_\perp = m_0 - m_2 \left[\frac{\partial^2}{\partial r^2} + \frac{1}{r}\frac{\partial}{\partial r}\right], \quad (C4)$$

and $m_\parallel = m_2(p_\phi^2 + p_z^2)$, with

$$p_\phi = -i\frac{1}{r}\frac{\partial}{\partial\phi}, \quad p_z = -i\frac{\partial}{\partial z}. \quad (C5)$$

We have also introduced $\hat{\boldsymbol{r}} = (\cos\phi, \sin\phi)$ and $\hat{\boldsymbol{\phi}} = (-\sin\phi, \cos\phi)$.

We then consider a solution of the eigenvalue equation,

$$H_\perp |\psi_\perp\rangle\rangle = E_\perp |\psi_\perp\rangle\rangle, \tag{C6}$$

of the form $\psi_\perp \sim e^{\kappa(r-R)}$, i.e., we set $p_r = -i\kappa$ ($\kappa > 0$) in Eq. (C2). $E_\perp$ is the value of the energy eigenvalue at the Dirac point. In order to cope with the boundary condition $|\psi_\perp\rangle_{r=R} = \mathbf{0}$ on the surface of the cylinder, one can verify that this must be zero ($E_\perp = 0$).[11,40] This implies

$$\tau_x H_\perp |\psi_\perp\rangle\rangle = \mathbf{0}. \tag{C7}$$

Notice that in the second line of Eq. (C2), $\hat{\boldsymbol{r}} \cdot \boldsymbol{\sigma}$ can be diagonalized by pointing the real-spin spinor in the direction of $\hat{\boldsymbol{r}}$ as Eqs. (8). Then, one can satisfy Eq. (C7) by four simultaneous eigenstates of τ_y and $\hat{\boldsymbol{r}} \cdot \boldsymbol{\sigma}$, i.e.,

$$|\psi_\perp\rangle\rangle = \rho(r)|\tau_z\pm\rangle|\hat{\boldsymbol{r}}\pm\rangle_{\mathrm{dv}}, \tag{C8}$$

if κ is a solution of

$$E_\perp = m_\perp \pm A\kappa = m_0 - m_2\kappa^2 \pm A\kappa = 0. \tag{C9}$$

Here, $|\hat{\boldsymbol{r}}\pm\rangle_{\mathrm{dv}}$ has been given in Eqs. (8). The double sign in Eq. (C9) signifies $+(-)$ when the combination of the two signs in $|\tau_y\pm\rangle|\hat{\boldsymbol{r}}\pm\rangle$ in Eq. (C8) are the same (opposite). One has to consider a linear combination of the eigenstates of the form

$$\rho(r) \sim e^{\kappa_1(r-R)} - e^{\kappa_2(r-R)}, \tag{C10}$$

where κ_1 and κ_2 are solutions of Eq. (C9) with $E_\perp = 0$, i.e.,

$$\kappa = \frac{\pm A \pm \sqrt{A^2 + 4m_0 m_2}}{4m_2} \equiv \kappa_{1,2}, \tag{C11}$$

where the double sign in front of A corresponds to the one in Eq. (C9). The second one is arbitrary, with each choice determining the subscript of $\kappa_{1,2}$. Here, the surface state should be localized in the inner vicinity of the surface of the cylinder. For that, one needs a solution of the form of

Eq. (C10) with $\kappa_{1,2}$ whose real parts are *both* positive. This is in one-to-one correspondence with

(i) the choice of $+$ sign in front of A in Eq. (C11), *assuming that A/m_2 is positive*, and

(ii) the condition $m_0 m_2 < 0$.

Thus, the two basis solutions that span the subspace of the surface solutions of Eq. (5) that are also compatible with the boundary condition are identified as $|\hat{\boldsymbol{r}}\pm\rangle\rangle_{\mathrm{dv}}$, introduced in Eqs. (7). For preciseness, we normalize Eq. (C10) as

$$\rho(r) = \sqrt{\frac{\kappa_1 \kappa_2 (\kappa_1 + \kappa_2)}{\pi R}} \frac{e^{\kappa_1(r-R)} - e^{\kappa_2(r-R)}}{|\kappa_1 - \kappa_2|}. \tag{C12}$$

Any surface solution $|\boldsymbol{\alpha}\rangle\rangle$ of Eq. (5), satisfying

$$H_\parallel |\boldsymbol{\alpha}\rangle\rangle = E|\boldsymbol{\alpha}\rangle\rangle, \tag{C13}$$

can be expressed as a linear combination of these two basis solutions as

$$|\boldsymbol{\alpha}\rangle\rangle = \alpha_+ |\boldsymbol{r}+\rangle\rangle_{\mathrm{dv}} + \alpha_- |\boldsymbol{r}-\rangle\rangle_{\mathrm{dv}}, \tag{C14}$$

or as in Eq. (9).

Finally, following the prescription of the standard degenerate perturbation theory, we consider the secular equation for Eq. (C13), i.e.,

$$\begin{bmatrix} \langle\langle \boldsymbol{r}+|H_\parallel|\boldsymbol{r}+\rangle\rangle & \langle\langle \boldsymbol{r}+|H_\parallel|\boldsymbol{r}-\rangle\rangle \\ \langle\langle \boldsymbol{r}-|H_\parallel|\boldsymbol{r}+\rangle\rangle & \langle\langle \boldsymbol{r}-|H_\parallel|\boldsymbol{r}-\rangle\rangle \end{bmatrix} \begin{bmatrix} \alpha_+ \\ \alpha_- \end{bmatrix} = E \begin{bmatrix} \alpha_+ \\ \alpha_- \end{bmatrix}, \tag{C15}$$

where we have omitted the subscript dv, for simplicity. We define the coefficient matrix $\langle\langle \boldsymbol{r}\pm|H_\parallel|\boldsymbol{r}\pm\rangle\rangle$ in the secular equation (C15) as the surface effective Hamiltonian H_{surf}. Noticing the relations such as

$$\langle \hat{\boldsymbol{r}}\pm|\hat{\boldsymbol{\phi}} \cdot \boldsymbol{\sigma}|\hat{\boldsymbol{r}}\pm\rangle = \sigma_y, \tag{C16}$$

$$\langle \hat{\boldsymbol{r}}\pm|\sigma_z|\hat{\boldsymbol{r}}\pm\rangle = \sigma_x, \tag{C17}$$

the explicit form of H_{surf} is found as given in Eq. (10).

---

[1] J. E. Moore, Nature (London) **464**, 194 (2010).

[2] M. Z. Hasan and C. L. Kane, Rev. Mod. Phys. **82**, 3045 (2010).

[3] Y. Zhang, K. He, C.-Z. Chang, C.-L. Song, L.-L. Wang, X. Chen, J.-F. Jia, Z. Fang, X. Dai, W.-Y. Shan, S.-Q. Shen, Q. Niu, X.-L. Qi, S.-C. Zhang, X.-C. Ma, and Q.-K. Xue, Nature Phys. **6**, 584 (2010).

[4] B. Zhou, H.-Z. Lu, R.-L. Chu, S.-Q. Shen, and Q. Niu, Phys. Rev. Lett. **101**, 246807 (2008).

[5] H.-Z. Lu, W.-Y. Shan, W. Yao, Q. Niu, and S.-Q. Shen, Phys. Rev. B **81**, 115407 (2010).

[6] J. Linder, T. Yokoyama, and A. Sudbø, Phys. Rev. B **80**, 205401 (2009).

[7] W.-Y. Shan, H.-Z. Lu, and S.-Q. Shen, New J. Phys. **12**, 043048 (2010).

[8] Y. Zhang and A. Vishwanath, Phys. Rev. Lett. **105**, 206601 (2010).

[9] P. M. Ostrovsky, I. V. Gornyi, and A. D. Mirlin, Phys. Rev. Lett. **105**, 036803 (2010).

[10] J. H. Bardarson, P. W. Brouwer, and J. E. Moore, Phys. Rev. Lett. **105**, 156803 (2010).

[11] K.-I. Imura, Y. Takane, and A. Tanaka, Phys. Rev. B **84**, 195406 (2011).

[12] L. Fu, C. L. Kane, and E. J. Mele, Phys. Rev. Lett. **98**, 106803 (2007).

[13] J. E. Moore and L. Balents, Phys. Rev. B **75**, 121306 (2007).

[14] R. Roy, Phys. Rev. B **79**, 195322 (2009).

[15] J. C. Y. Teo and C. L. Kane, Phys. Rev. B **82**, 115120 (2010).

[16] Y. Ran, arXiv:1006.5454.

[17] Y. Ran, Y. Zhang, and A. Vishwanath, Nature Phys. **5**, 298 (2009).

[18] K.-I. Imura, Y. Takane, and A. Tanaka, Phys. Rev. B **84**, 035443 (2011).

[19] R. S. K. Mong, J. H. Bardarson, and J. E. Moore, Phys. Rev. Lett. **108**, 076804 (2012).

[20] Z. Ringel, Y. E. Kraus, and A. Stern, Phys. Rev. B **86**, 045112 (2012).

[21] C.-X. Liu, X.-L. Qi, H. J. Zhang, X. Dai, Z. Fang, and S.-C. Zhang, Phys. Rev. B **82**, 045122 (2010).

[22] H. Zhang, C.-X. Liu, X.-L. Qi, X. Dai, Z. Fang, and S.-C. Zhang, Nature Phys. **5**, 438 (2010).

[23] L. Fu and C. L. Kane, Phys. Rev. B **76**, 045302 (2007).

[24] D. Hsieh, Y. Xia, D. Qian, L. Wray, Y. S. Hor, R. J. Cava, and M. Z. Hasan, Nature (London) **452**, 970 (2008).

[25] H.-J. Noh, H. Koh, S.-J. Oh, J.-H. Park, H.-D. Kim, J. D. Rameau, T. Valla, T. E. Kidd, P. D. Johnson, Y. Hu, and Q. Li, Europhys. Lett. **81**, 57006 (2008).

[26] T. Sato, K. Segawa, H. Guo, K. Sugawara, S. Souma, T. Takahashi, and Y. Ando, Phys. Rev. Lett. **105**, 136802 (2010).

[27] K. Kuroda, M. Ye, A. Kimura, S. V. Eremeev, E. E. Krasovskii, E. V. Chulkov, Y. Ueda, K. Miyamoto, T. Okuda, K. Shimada, H. Namatame, and M. Taniguchi, Phys. Rev. Lett. **105**, 146801 (2010).

[28] Z. Ren, A. A. Taskin, S. Sasaki, K. Segawa, and Y. Ando, Phys. Rev. B **82**, 241306 (2010).

[29] K. Nomura, M. Koshino, and S. Ryu, Phys. Rev. Lett. **99**, 146806 (2007).

[30] J. H. Bardarson, J. Tworzydło, P. W. Brouwer, and C. W. J. Beenakker, Phys. Rev. Lett. **99**, 106801 (2007).

[31] H. Peng, K. Lai, D. Kong, S. Meister, Y. Chen, X.-L. Qi, S.-C. Zhang, Z.-X. Shen, and Y. Cui, Nature Mater. **9**, 225 (2010).

[32] D. Hsieh, Y. Xia, D. Qian, L. Wray, J. H. Dil, F. Meier, J. Osterwalder, L. Patthey, J. G. Checkelsky, N. P. Ong, A. V. Fedorov, H. Lin, A. Bansil, D. Grauer, Y. S. Hor, R. J. Cava, and M. Z. Hasan, Nature (London) **460**, 1101 (2009).

[33] E. Prodan, Phys. Rev. B **83**, 195119 (2011).

[34] K. Ebihara, K. Yada, A. Yamakage, and Y. Tanaka, Physica E **44**, 885 (2012).

[35] M. R. Zirnbauer, J. Math. Phys. **37**, 4986 (1996).

[36] A. P. Schnyder, S. Ryu, A. Furusaki, and A. W. W. Ludwig, Phys. Rev. B **78**, 195125 (2008).

[37] A. Kitaev, AIP Conf. Proc. **1134**, 22 (2009).

[38] A. P. Schnyder, S. Ryu, A. Furusaki, and A. W. W. Ludwig, AIP Conf. Proc. **1134**, 10 (2009).

[39] S. Ryu, A. P. Schnyder, A. Furusaki, and A. W. W. Ludwig, New J. Phys. **12**, 065010 (2010).

[40] K.-I. Imura, Y. Yoshimura, Y. Takane, and T. Fukui, Phys. Rev. B **86**, 235119 (2012).

[41] M. Zubkov and G. Volovik, Nucl. Phys. B **860**, 295 (2012).

[42] M. A. Zubkov, Phys. Rev. B **86**, 034505 (2012); arXiv:1202.2524.

[43] K.-I. Imura, A. Yamakage, S. Mao, A. Hotta, and Y. Kuramoto, Phys. Rev. B **82**, 085118 (2010).

[44] M. König, H. Buhmann, L. W. Molenkamp, T. Hughes, C.-X. Liu, X.-L. Qi, and S.-C. Zhang, J. Phys. Soc. Jpn. **77**, 031007 (2008).

[45] K.-I. Imura and Y. Takane (unpublished).